Available online at www.sciencedirect.com
SCIENCE DIRECT®
Composites Science and Technology 63 (2003) □–□
COMPOSITES SCIENCE AND TECHNOLOGY
www.elsevier.com/locate/compscitech

Three-dimensional viscoelastic simulation of woven composite substrates for multilayer circuit boards

Qi Zhu[a,1], Pranav Shrotriya[b,2], Nancy R. Sottos[b], Philippe H. Geubelle[a,*]

[a]Department of Aeronautical and Astronautical Engineering, University of Illinois at Urbana-Champaign, MC 236 306 Talbot Laboratory, 104 South Wright Street, Urbana, IL 61801, USA
[b]Department of Theoretical and Applied Mechanics, University of Illinois at Urbana-Champaign, Urbana, IL 61801, USA

Received 10 July 2001; received in revised form 7 January 2003; accepted 20 March 2003

Abstract

Viscoelastic properties of woven composite substrates are essential to design dimensionally stable multilayer printed circuit boards. Unlike most existing numerical work which rely on simplified constitutive (elastic) and geometrical models, this study involves a fully three-dimensional viscoelastic model of a plain weave composite with accurate characterization of the woven geometry. Comparisons between numerical predictions and experimental data clearly indicate that the creep compliance of the composite depends not only on the relaxation of the matrix, but also on the time-dependent flexural deformations of the woven fabric bundles. Predictions of the inhomogeneous deformation fields over the repeating cell agree with experimental observations.

Keywords: Woven composites

1. Introduction

Multilayer printed circuit boards (PCB) are used extensively in electronic packaging assemblies. The boards, shown schematically in Fig. 1, consist of multiple layers of woven glass/epoxy composite substrate sandwiched between copper foils. Manufacture of multilayer circuit boards consists of several stages. In the first stage, glass fibers are woven into a plain weave fabric consisting of two fiber bundles in orthogonal directions, which alternately pass over and under each other. The bundles that emerge perpendicular to the weaving loom are called warp bundles while the parallel bundles are called the fill or weft. A schematic of the plain weave fabric is shown in Fig. 2. The glass fiber fabric is impregnated with FR-4 epoxy resin to form a B-staged prepreg and typically one or two B-stage prepreg layers are then consolidated between two layers of copper foil in a hot press to form a C-staged core. The cores go through a series of etching and screening processes. Multilayer boards are fabricated by relaminating alternating layers of B-staged prepreg, which act as bonding sheets, and C-stage cores.

A large number of plain weave fabric styles are currently used in circuit board design. The fabric styles are often unbalanced, i.e., the warp and fill directions include different numbers of fiber bundles or different size fiber diameters. Because of the variation in fiber bundle sizes, geometry of the undulating fiber bundles is different and depends on the fabric styles. Hence, composite substrates with different fabric styles have very different properties. Furthermore, the same fabric style has different properties in the warp and fill directions. Sottos et al. [1] measured significant differences in the fabric geometry (bundle size, crimp, etc.), the elastic moduli, and coefficients of thermal expansion (CTE) in the warp and fill directions of two common substrates for multilayer circuit boards. Wu et al. [2] and Yuan and Falanga [3] characterized the CTE of substrates below the matrix glass transition temperature (T_g) and detected higher CTE values in the fill direction. During relamination, the boards are heated above the matrix

* Corresponding author. Tel.: +1-217-244-7648; fax: +1-217-244-0720.
E-mail address: geubelle@uiuc.edu (P.H. Geubelle).
[1] Present address: General Electric Corporate Research and Development, Niskayuna, NY 12309, USA.
[2] Present address: Department of Mechanical and Aerospace Engineering, Princeton University, Princeton, NJ 08544, USA.

0266-3538/03/$ - see front matter © 2003 Published by Elsevier Ltd.
doi:10.1016/S0266-3538(03)00171-4

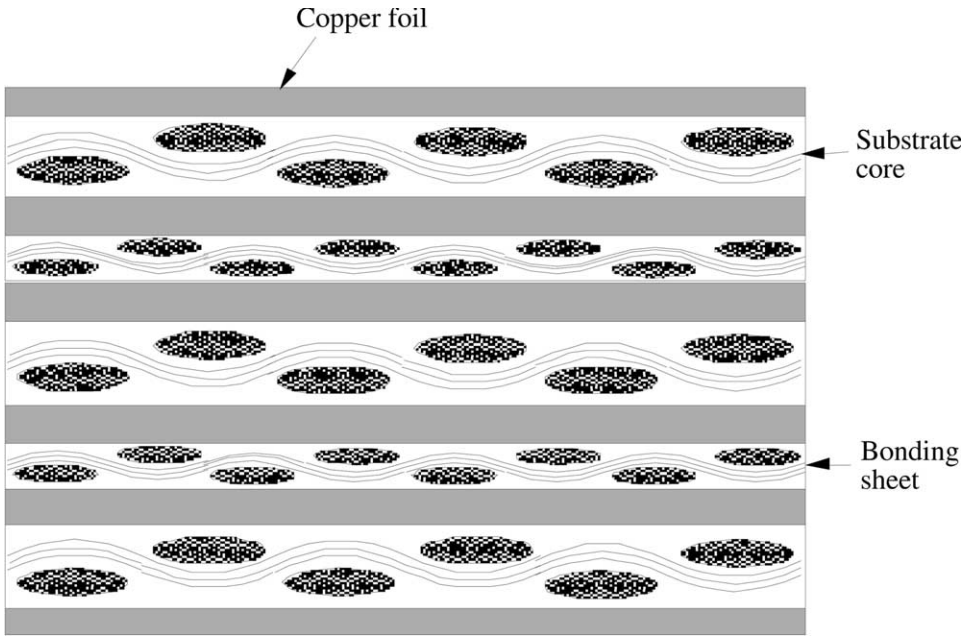

Fig. 1. Schematic of a multilayer circuit board.

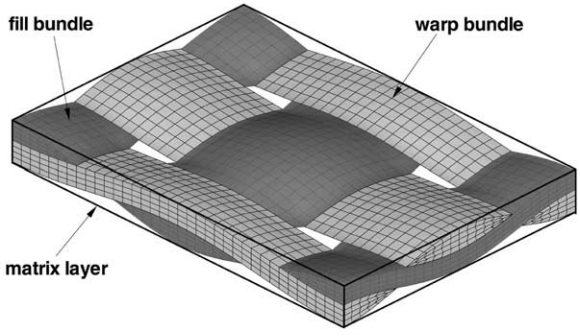

Fig. 2. Schematic of a plain weave fabric.

glass transition temperature for an extended period of time. At temperatures near the glass transition, viscoelastic processes dominate the matrix response and result in time-temperature dependence of substrate properties. Wang et al. [4] generated master relaxation curves for a 109 style composite substrate and reported different relaxation responses in the warp and fill directions. Shrotriya and Sottos [5] characterized the fabric architecture and creep compliance of a 7628 style composite substrate and correlated the different material responses along the warp and fill directions to the differences in fabric architecture. Given the large number of different fabric styles used in the circuit board industry and the strong influence of weave architecture, further investigation is required to characterize the substrate creep and relaxation behavior with respect to different fabric styles. Since experimental viscoelastic characterization is not viable for every fabric style, micro-mechanical models are essential to predict the substrate properties from fiber, matrix and fabric properties.

A myriad of micro-mechanical models for prediction of the elastic properties of woven composites have been reported in the literature. Tan et al. [6] and Kuhn and Charalambides [7,8] presented an exhaustive literature survey on elastic micro-mechanical models for woven composites. In comparison, there are only a few reported micro-mechanical models for viscoelastic response of woven composites. Govindarajan et al. [9] utilized the elastic-viscoelastic principle to extend an existing elastic model [10] for prediction of creep behavior of graphite/epoxy woven composite. They characterized the creep compliance of the composite, but were unable to measure the matrix response directly. Instead, they determined the matrix response by fitting predictions to the measured creep compliance.

In related work, Shrotriya and Sottos [5,12] have used two different approaches—elastic viscoelastic correspondence principle and two-dimensional (2-D) finite element analysis—to predict the viscoelastic response of a woven composite from fabric, fiber and matrix properties. The analytical models based on the elastic–viscoelastic correspondence principle required minimal computational effort in order to predict the composite response, but suffered from implicit assumptions about the boundary conditions and deformation of the composite. The micro-mechanical models predicted an unrelaxed modulus close to the experimental value but underpredicted the relaxation of the composite. Comparisons of the model predictions with the experimental data indicated that the relaxation modulus of the composite is dependent not only on the relaxation of the matrix but also on flexural deformation of the woven fabric bundles and boundary conditions of the unit cell.

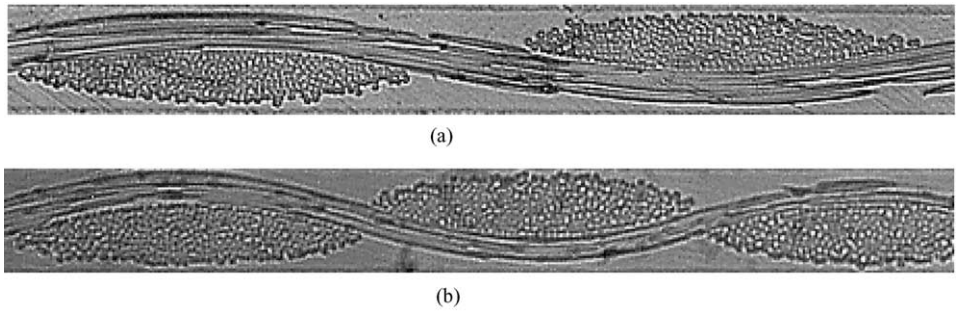

Fig. 3. Photomicrograph of 7628 laminate (100×). (a) The warp and fill yarns are parallel and perpendicular to the page, respectively. (b) The fill and warp yarns are parallel and perpendicular to the page, respectively.

In the second approach, plane strain finite element analysis was utilized to predict the creep compliance of the composite. The compliance was predicted for two different boundary conditions: traction-free in order to model the experiments, and symmetric with flat surfaces as a limiting case of the boundary conditions imposed in the analytical model. Predictions corresponding to traction-free boundary conditions approximated the general trends of experimental curves but did not accurately match the initial unrelaxed compliance, fully relaxed compliance and retardation spectrum of the compliance curves.

The current article presents the results of a three-dimensional (3-D) finite element model utilized to predict the viscoelastic response of the woven composite substrate. Model predictions are compared with experimentally measured response in order to understand the influence of interlaced bundle architecture on the composite response. The computed deformation fields are also compared with moire images of the unit cell [12,13] in order to validate the physical basis of modelling assumptions and elucidate the influence of flexural deformation on composite response.

The article begins with a brief discussion of the fabric, fiber bundle and matrix properties used to predict the constitutive response of the composite. The next three sections present the development and implementation of the finite element model, mesh generation and discussion on boundary conditions on the composite unit cell. The article concludes with a discussion of the numerical results. Creep compliance predictions and unit cell deformation fields for the woven composite are compared with reported experimental measurements [5,12,13].

2. Fabric, fiber bundles and matrix properties

The composite substrate consists of FR-4 epoxy matrix reinforced with a plain weave glass fabric. In a previous work, Shrotriya and Sottos [5] characterized the fabric architecture and viscoelastic properties of 7628 style composite substrate. Photomicrographs taken in the warp and fill directions are shown in Fig. 3.

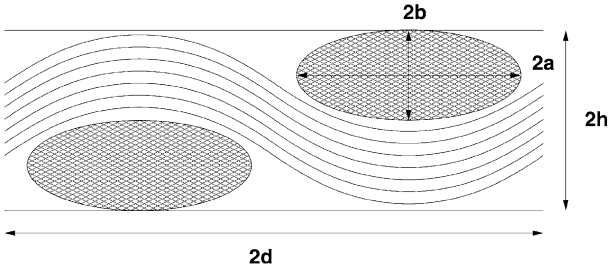

Fig. 4. Schematic of plain weave geometry.

The warp and fill bundles have different sizes and crimp angles, which are described by a, b, d, and h (see Fig. 4 and Table 1). They reported the creep compliances as well as stress relaxation moduli of the neat FR-4 epoxy matrix and composite substrate in the warp and fill directions. They indicated that horizontal shifting of the creep data obtained at different temperatures alone was adequate to form the master creep compliance curves. Therefore, following Wang et al. [14], it was assumed that both the epoxy and composite were thermorheologically simple. In addition, the logarithm of the shift function for the matrix and the composite substrate in the warp and fill directions had similar behavior and were fit to a bi-linear equation

$$\log_{10}[a_T(T)] = \begin{cases} -5757/T + 19, & T < 393\ \text{K}, \\ -20661/T + 57, & T > 393\ \text{K}. \end{cases} \quad (1)$$

The material properties of FR-4 epoxy and glass fibers are represented in Tables 2 and 3.

In the current work, the relaxation moduli of the FR-4 epoxy and of a straight, unidirectional fiber bundle (without undulation) are used in the finite element

Table 1
Measurements of bundle sizes, crimp, and fiber volume fractions [12]

	Aspect ratio a/b	Crimp b/d	Fiber volume fraction in bundle	Fiber volume fraction in composite
Fill	7.26	0.083	0.75	0.19
Warp	5.26	0.053	0.75	0.26

Table 2
Moduli and Poisson's ratio of FR-4 epoxy and glass fiber [5]

	Elastic modulus E^{u} (GPa)	Equilibrium modulus E^{∞} (GPa)	Poisson's ratio v
FR-4 epoxy	2.9	0.12	0.33
Glass fiber	72.3	–	0.22

Table 3
Relaxation times and weight factors for FR-4 epoxy [5]

i	λ_i (min)	W_i
1	5.32	0.0641
2	3.61e2	0.0759
3	5.39e3	0.0482
4	2.53e4	0.0804
5	1.91e5	0.1307
6	1.46e6	0.2020
7	7.70e6	0.1978
8	4.25e7	0.0936
9	2.16e8	0.0509
10	1.93e9	0.0560

model to determine the creep compliances of the woven composite. The effect of the bundle undulation is not reflected in the bundle properties, but captured by the geometrical model. The viscoelastic properties of a straight, transversely isotropic fiber bundle are calculated using the elastic-viscoelastic correspondence principle and the micro-mechanical relations based on self-consistent field method (see Appendix) combining the FR-4 matrix and elastic glass fiber properties (Table 2). As listed in Table 1, the fiber volume fraction of the bundle is 0.75 in the fill and warp directions. The relaxation times and weight factors of the bundle are found to be very close to those of the matrix in Table 3, and the shift functions for the bundle are the same as those of the epoxy in Eq. (1). The resulting unrelaxed and fully relaxed material properties for a straight bundle are listed in Table 4.

3. Viscoelastic stress model

3.1. Constitutive equations

The constitutive equation for an anisotropic linearly viscoelastic material under isothermal condition is [15],

$$\sigma_{ij}(t)=\int_{-\infty}^{t} Q_{ijkl}(T,\, t-t')\frac{\partial \epsilon_{kl}(t')}{\partial t'}\mathrm{d}t'(i,j,k,l=1,2,3), \quad (2)$$

where σ_{ij} are the stress components, ϵ_{kl} the strains, and Q_{ijkl} the relaxation moduli. We assume that the material

Table 4
Moduli and Poisson's ratios of a straight fiber bundle

	Elastic values	Fully relaxed values
E_{11} (GPa)	59.1	58.6
E_{22} (GPa)	27.3	1.8
G_{12} (GPa)	7.8	0.43
G_{23} (Gpa)	12.4	0.88
v_{12}	0.24	0.24

shows thermorheologically simple behavior and is strain-free before $t=0$. (2) can then be written as

$$\sigma_{ij}(t)=\int_0^t Q_{ijkl}(\xi-\xi')\frac{\partial \epsilon_{kl}(t')}{\partial t'}\mathrm{d}t', \quad (3)$$

with the reduced times ξ and ξ' defined as

$$\xi=\int_0^t a_T(T)\mathrm{d}t'', \qquad \xi'=\int_0^{t'} a_T(T)\mathrm{d}t'' \quad (4)$$

The stress relaxation modulus for a thermorheologically simple material is approximated by M Maxwell elements as

$$E(\xi)=E^{\infty}+E^{*}\sum_{i=1}^{M} W_i \exp\left(-\frac{\xi}{\lambda_i}\right), \quad (5)$$

where $E^{*}=E^{u}-E^{\infty}$ is a material constant, E^{∞} the fully relaxed modulus (equilibrium modulus), E^{u} the unrelaxed modulus, W_i the weight factors, and λ_i the discrete relaxation times. This Prony series model provides computational convenience in temperature–time–superposition integration calculations. In particular, it allows us to use a recursive formulation to solve the viscoelastic integral equation, as first proposed by Taylor et al. [16] and described in Section 3.2.2.

3.2. Finite element implementation

3.2.1. Finite element formulation

Expanding on Lin and Yi's generalized plane-strain formulation [17], a 3-D finite element formulation is developed starting from the variational theorem for linear viscoelastic materials given by Christensen [18]

$$\delta\Pi = \int_v \int_{t'=0}^{t'=t}\int_{t''=0}^{t''=t-t'} Q_{ijkl}(T,\, t-t'-t'')\frac{\partial \epsilon_{kl}(t'')}{\partial t''}\mathrm{d}t''\frac{\partial \delta\varepsilon_{ij}(t')}{\partial t'}\mathrm{d}t'\mathrm{d}V - \int_{S_{tr}}\int_{t'=0}^{t'=t} T_{tr_i}(t-t')\frac{\partial \delta u_i(t')}{\partial t'}\mathrm{d}t'\mathrm{d}S_{tr}=0. \quad (6)$$

In the above equation, we assume the structure to be strain-free before $t=0$.

We interpolate the time-dependent displacement field $u(\mathbf{X}, t)$ and total strain field $\epsilon(\mathbf{X},t)$ using the shape functions $\mathbf{N}(\mathbf{X})$ and the nodal displacement vector $\mathbf{u}(t)$ as

$$u(\mathbf{X}, t) \approx \mathbf{N}(\mathbf{X})\mathbf{u}(t), \qquad \boldsymbol{\epsilon}(\mathbf{X}, t) \approx \mathbf{B}(\mathbf{X})\mathbf{u}(t), \tag{7}$$

where $\mathbf{B}$ contains partial derivatives of the shape functions $\mathbf{N}$ with respect to $\mathbf{X}$. Substituting (7) into the variational expression (6), then transforming it to the temperature–time-superposition domain, and substituting the material model (5), we obtain the finite element formulation for the viscoelastic problem

$$\int_0^t \left[\mathbf{K}^{\infty} + \sum_{i=1}^{M} \mathbf{K}_i^{*} \exp\left(-\frac{\xi - \xi'}{\lambda_i}\right)\right] \frac{\partial \mathbf{u}(t')}{\partial t'} \mathrm{d}t' = \mathbf{F}^{\mathrm{tr}}(t) \tag{8}$$

where

$$\mathbf{K}^{\infty} = \int_V \mathbf{B}^T \mathbf{Q}^{\infty} \mathbf{B} \mathrm{d}V, \qquad \mathbf{K}_i^{*} = \int_V \mathbf{B}^T W_i \mathbf{Q}^{*} \mathbf{B} \mathrm{d}V, \tag{9}$$

$$\mathbf{F}^{\mathrm{tr}}(t) = \int_{S_{\mathrm{tr}}} N^T T_{\mathrm{tr}}(t) \mathrm{d}S_{\mathrm{tr}}. \tag{10}$$

In the above equations, $\mathbf{Q}^{\infty}$ and $\mathbf{Q}^{*}$ correspond to the element stiffness matrices computed by E^{∞} and E^{*} introduced in Eq. (5), respectively.

Similarly, substitution of the relaxation modulus (5) into the constitutive Eq. (3) yields the following form of the stress vector

$$\boldsymbol{\sigma}(t) = \int_0^t \left[\mathbf{Q}^{\infty} + \sum_{i=1}^{M} W_i \mathbf{Q}^{*} \exp\left(-\frac{\xi - \xi'}{\lambda_i}\right)\right] \frac{\partial \boldsymbol{\epsilon}(t')}{\partial t'} \mathrm{d}t'. \tag{11}$$

3.2.2. Recursive scheme

A direct integration of (8) would require enormous computing time and memory storage owing to the hereditary integrals resulting from the viscoelastic model. Taylor's recursive scheme [16] is applied here to overcome these difficulties. In this numerical procedure, the displacement is assumed to be piecewise linear during each time interval $t_{n-1} \leqslant t \leqslant t_n$:

$$\frac{\partial \mathbf{u}(t)}{\partial (t)} \approx \frac{\mathbf{u}(t_n) - \mathbf{u}(t_{n-1})}{t_n - t_{n-1}}. \tag{12}$$

Substitution of (12) into (8) yields the following linear relations in terms of the displacement increment $\Delta\mathbf{u}(t_n)$

$$\hat{\mathbf{K}} \Delta \mathbf{u}(t_n) = \hat{\mathbf{F}}_1 + \hat{\mathbf{F}}_2, \tag{13}$$

with

$$\hat{\mathbf{K}} = \mathbf{K}^{\infty} + \sum_{i=1}^{M} \mathbf{K}_i^{*} h_i(t_n), \tag{14}$$

$$\hat{\mathbf{F}}_1 = -\left[\mathbf{K}^{\infty} \mathbf{u}(t_{n-1}) + \sum_{i=1}^{M} \boldsymbol{g}_i(t_n)\right], \tag{15}$$

$$\hat{\mathbf{F}}_2 = \mathbf{F}^{\mathrm{tr}}(t_n), \tag{16}$$

where $h_i(t_n)$ is an internal variable defined as

$$h_i(t_n) = \frac{1}{\Delta t_n} \int_{t_{n-1}}^{t_n} \exp\left(-\frac{\xi(t_n) - \xi'}{\lambda_i}\right) \mathrm{d}t', \tag{17}$$

and $\boldsymbol{g}_i(t_n)$ is given recursively by

$$\boldsymbol{g}_i(t_n) = \exp\left(-\frac{\Delta\xi(t_n) - \xi'}{\lambda_i}\right) \left[\mathbf{g}_i(t_{n-1}) + \mathbf{K}_i^{*} h_i(t_{n-1}) \Delta\mathbf{u}(t_{n-1})\right]. \tag{18}$$

The initial values to be used in the recursive scheme are

$$h_i(0) = 1, \qquad \mathbf{g}_i(0) = 0, \qquad \Delta\mathbf{u}(0) = \mathbf{u}(0). \tag{19}$$

Applying the same approach as for (1), we obtain a recursive formulation for the constitutive equation,

$$\boldsymbol{\sigma}(t_n) = \mathbf{Q}^{\infty} \boldsymbol{\epsilon}(t_n) + \sum_{i=1}^{M} W_i \mathbf{Q}^{*} h_i(t_n) \Delta\boldsymbol{\epsilon}(t_n) + \sum_{i=1}^{M} \boldsymbol{g}_i'(t_n), \tag{20}$$

with

$$\boldsymbol{g}_i'(t_n) = \exp\left(-\frac{\Delta\xi t_n}{\lambda_i}\right) \left[\boldsymbol{g}_i'(t_{n-1}) + W_i \mathbf{Q}^{*} h_i(t_n) \Delta\boldsymbol{\epsilon}(t_{n-1})\right], \tag{21}$$

$$\boldsymbol{g}_i'(0) = \mathbf{0}, \Delta\boldsymbol{\epsilon}(0) = \boldsymbol{\epsilon}(0). \tag{22}$$

Once the nodal displacement vector $\mathbf{u}(t_n) = \boldsymbol{u}(t_{n-1}) + \Delta\boldsymbol{u}(t_n)$ is obtained, we can calculate the stresses in each element from (20) to (22) together with the strain–displacement relation (7).

Various verification problems have been carried out to test the correctness of the finite element code [19,20]. For 3-D elastic problems, our results match those obtained by the commercial software ABAQUS™ very well. For viscoelastic problems, the finite element solution agrees with the analytical solution obtained using the elastic-viscoelastic correspondence principle.

4. Mesh generation

The geometry of the plain weave composite can be completely characterized through consideration of the smallest representative volume element within a composite laminate, namely, the symmetric unit cell. A 3-D solid model was developed using MATHEMATICA™ (Wolfram Research, Urbana, IL) to approximate the

geometry of the unit cell. Following the procedure described by Naik [21], trigonometric functions and geometric parameters of the 7628 style fabric (shown in Table 1), were utilized to define the 3-D undulating surfaces bounding the interlacing bundles. The bounding surfaces were determined such that the warp and fill bundles did not interpenetrate each other. The volume enclosed by the bounding surfaces was discretized using brick elements. Fig. 5 shows the finite element discretization of the unit cell of 7628 style composite substrate using eight-node brick elements with $2\times2\times2$ integration points.

5. Boundary conditions

The approach for computing the compliance of the plain weave composite is illustrated in Fig. 6(a). A unit uniform traction is applied to the lamina. Two adjacent unit cells are aligned along the loading direction. Symmetry boundary conditions are applied on two sides of the domain, and all the other surfaces are traction free. The compliance is then calculated by averaging the normal strains of half of the nodes on the adjacent surface of the two unit cells (from A to B). As illustrated in Fig. 6(a), although the surface where the loading is applied exhibits large variations in displacement due to the heterogeneity in the woven microstructure, the deformations on the adjacent surface of the two unit cell (along line AB) are quite uniform.

In Fig. 6(a), the left surface of the model is set free to allow the in-plane contraction of the lamina in the direction perpendicular to the loading. It means that the compliance determined in this way is actually the value near the free edge, and may not be exactly the same value

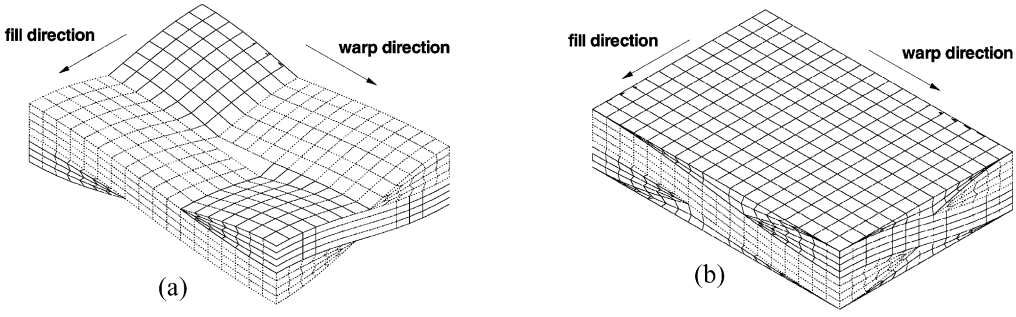

Fig. 5. Finite element discretization of a unit cell of 7628 style composite: (a) without the matrix layer, (b) with the matrix layer.

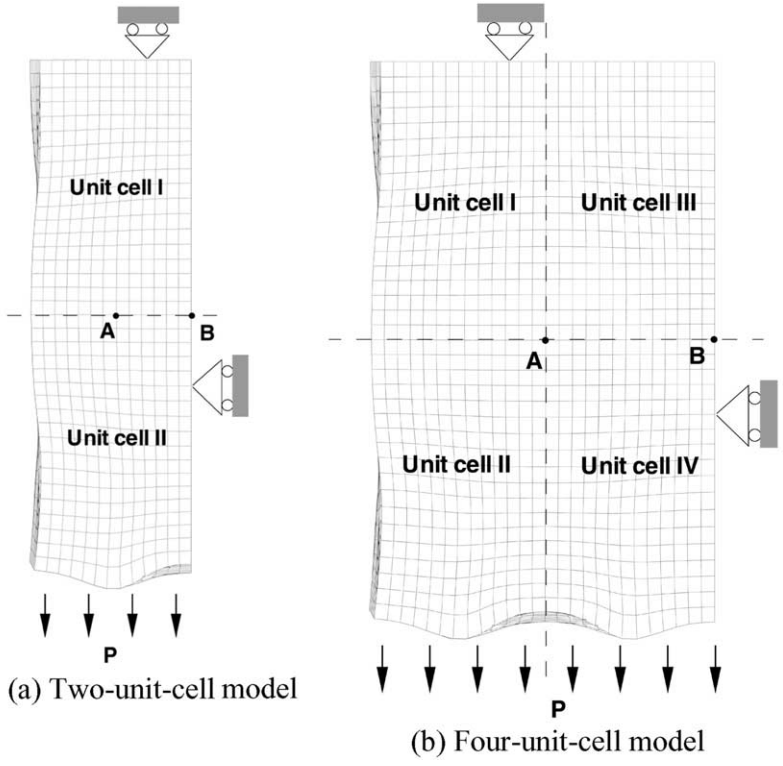

Fig. 6. Schematic of compliance calculation and the deformed shape of the plain weave lamina when loaded in the warp direction.

as the compliance of a plane weave lamina. To examine the edge effect, four unit cells are symmetrically arranged to form a repeating-unit model [Fig. 6(b)]. The compliance is obtained by averaging the normal strains of the nodes on the adjacent surface of the unit cells III and IV [from A to B in Fig. 6(b)]. The elastic compliance of the composite in the warp direction is computed using both the two-unit-cell and four-unit-cell models. The difference between the two results is found to be less than 1% (Table 5).

Mesh convergence is checked by comparing the elastic compliance of the plain weave composite in the warp direction obtained using eight- and twenty-node brick elements. As illustrated in Table 5, convergence has been achieved.

6. Result discussion

6.1. Creep compliance

To create the master creep compliance curves of the woven composite numerically, a unit load is applied successively in the fill and warp directions to the two-unit-cell model, as illustrated in Fig. 6(a). The loading is held for a short duration of time (10 min) at a constant temperature. The strain history is then recorded and plotted on the reduced time domain using the experimentally determined shift factors given by Eq. (1). The procedure repeats for different temperatures ranging from 25 to 170° C, thus forming the master compliance curves for the composite at reference temperature $T = 30°$ C.

Predicted master curves are compared with experimental data in Figs. 7 and 8, for the fill and warp directions, respectively. To ascertain the importance of bundle response in predicting the creep behavior of the composite, an extreme case in which the bundles are purely elastic (no relaxation) is also simulated. Shrotriya and Sottos [12] also predicted the creep compliance for the same composite using a 2-D plane–strain viscoelastic finite element model to model the cross-section of the lamina (see Fig. 3). The thickness of the longitudinal bundle was adjusted to preserve the corresponding bundle volume fraction of the real composite. The 2-D results are also plotted in Figs. 7 and 8 to compare with the 3-D predictions.

Table 5
Elastic compliance of the composite in the warp direction calculated using different models

Model	Element type	Number of elements	Number of nodes	Compliance (GPa)
Two-unit-cell	Eight-node brick	6432	7486	0.04266
Four-unit-cell	Eight-node brick	12 864	14 543	0.04227
Two-unit-cell	20-node brick	6432	28 831	0.04297

In the glassy or unrelaxed regime (10^{-2}–10^{1} min) of the creep compliance curves, numerical results are close to the experimental values, which shows that the finite element models are able to predict the predominantly elastic compliance of the composite fairly accurately. The 3-D model appears to be better than the 2-D model in predicting the elastic behavior of the composite because it captures the interlaced bundle architecture and varying cross section along the transverse direction. Both experimental and numerical results clearly indicate that the composite is softer in the fill direction than in the warp direction. This anisotropy is due to the higher bundle crimp and lower fiber volume fraction in the composite in the fill direction (Table 1).

In the transition region, when the bundle response is assumed to be purely elastic, the predicted creep compliance curves of the composite exhibit almost no relaxation. For the case of viscoelastic bundle response,

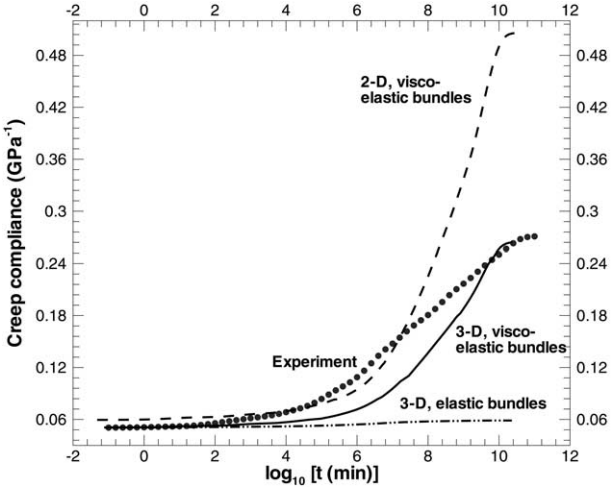

Fig. 7. Comparison between measured and predicted creep compliances in the fill direction. Reference temperature = 30 °C.

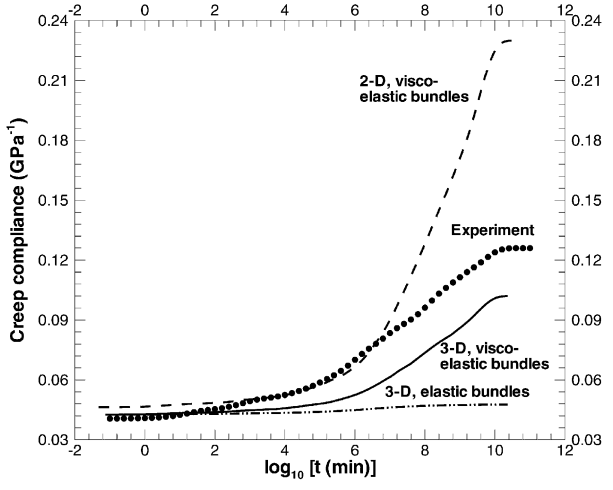

Fig. 8. Comparison between measured and predicted creep compliances in the warp direction. Reference temperature = 30 °C.

the predicted curves exhibit significant relaxation. This fact evidently reveals the dominant role of bundle viscoelastic response in the creep behavior of the composite.

When the viscoelastic bundle response is incorporated in the model, the predicted curves obtained by the 3-D model capture the general trends and magnitudes of the experimental data. However, the time dependence (retardation spectrum) of the numerical predictions and experimental data are clearly different. In the transition region, the numerical model underestimates the creep compliance in both the fill and warp directions. Moreover, the predicted curves seem to relax slower than the experimental ones.

The 3-D model predicts lower creep compliance than the 2-D model over the entire relaxation regime of the composite in both the fill and warp directions. Furthermore, the deviation between these two predictions increases when the material approaches the fully relaxed regime. The fully relaxed compliance predicted by the 2-D model is about twice as large as the experimental data in both the fill and warp directions. The 3-D model, however, captures the fully relaxed compliance in the fill direction, but underestimates the fully relaxed compliance in the warp direction. Overall, the 3-D model shows better agreement with experimental observations. The comparisons between 2-D and 3-D results indicate a strong 3-D effect in the woven composites due to the complex woven architecture and the constraint between the interlaced bundles.

To provide some insight into the time-dependence behavior of the composite, we compare, in Fig. 9, the normalized values of the numerical and experimental creep compliances of the matrix and composite. The numerical results are obtained using the 3-D model with viscoelastic bundle response. The normalized compliance $C_{\text{normalized}}$ is calculated from the unrelaxed (elastic) value C^{u} and the equilibrium (fully relaxed) value C^{∞} by

$$C_{\text{normalized}} = \frac{C(t) - C^{\text{u}}}{C^{\infty} - C^{\text{u}}} \tag{23}$$

As discussed earlier, the bundle viscoelastic response is calculated based on the matrix properties, thus they both have the same retardation spectrum. As clearly shown in Fig. 9, the time dependence of the composite is different from that of the matrix and bundles. The experimental observations indicate that the composite relaxes faster than its individual components, i.e. the matrix and bundles. Furthermore, the relaxation appears to take place faster in the warp direction than in the fill direction. These two phenomena are both captured by the 3-D model.

It is well known that the surface of a reinforcement or filler has a measurable effect on the molecular and segmental mobility of a polymer matrix [22]. As a result,

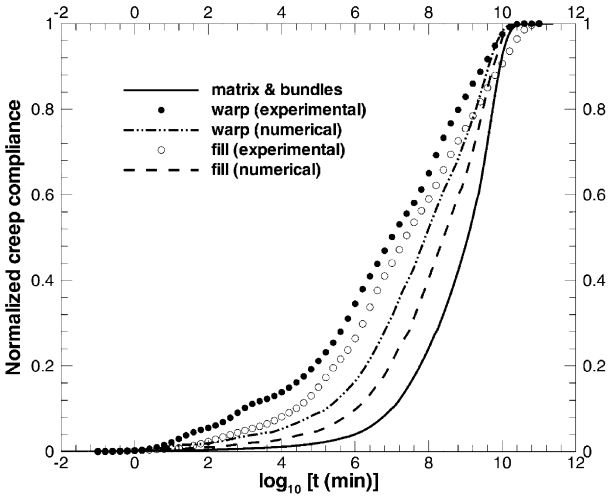

Fig. 9. Normalized creep compliances of the matrix and woven composite.

the mechanical properties and relaxation may be influenced by the presence of the reinforcement. Several researchers have observed differences in the relaxation or retardation spectra of a polymer matrix composite compared with that of the neat resin. Lipatov et al. [23] was among the first to report changes in the relaxation time spectral of filled polymer systems as a function of filler concentration. The average relaxation time of filled samples was shifted over two decades in time from unfilled samples. This shift was attributed to a selective sorption of one of the epoxy components on the filler surface before hardening. A surplus of the other component acted as plasticizer, causing a reduction of elastic modulus and a change in the relaxation behavior of the filled system. Similarly, Crowson and Arridge [24] observed a change in glass transition temperature between filled and unfilled epoxy systems. More recently, Palmese and McCullough [25] showed that a stoichiometric imbalance of epoxy resin and amine curing agent develops near fiber surfaces. For amine concentrations both above and below the stoichiometric point, the glass transition temperature of the polymer in that region was substantially reduced. Interferometric measurements reported by Sottos and Swindeman [26] for the same epoxy system indicated that a reduction in glass transition temperature near the fiber interface significantly influenced the time dependence of thermal deformations near the fiber surface.

Sullivan et al. [27] measured the retardation spectra of two different epoxies and their composites. They demonstrated that within the unrelaxed (glassy) and adjacent transition region, the spectra of the matrix and composites are similar to each other within a multiplicative constant, The presence of fibers alters only the magnitude component of the retardation spectrum but not the retardation time distribution component. However, at longer times, fibers are expected to affect the

viscoelastic spectra of a resin system. They showed that the peak of the retardation spectra of the composite was shifted from that of the matrix because the presence of fibers suppresses the longer time retardation mechanisms of the matrix. But these changes are unable to be captured by the viscoelastic micro-mechanical relation.

Given the high volume fraction of fibers in the bundles (approximately 75%), there is an increased probability for surface effects to dominate the viscoelastic response. Motivated by the shifts reported by Sullivan et al. [27], we modified the bundle response by shifting its peak relaxation spectrum to the left by two decades. The normalized initial and modified relaxation moduli of the bundle are shown in Fig. 10, and its material constants are listed in Table 6. As illustrated in Fig. 11, the predicted creep compliance curves obtained using the modified bundle response are in much better correlation with experimental observation. From the unrelaxed regime up to the transition region before 10^7 min, the numerical predictions agree with the experimental data very well. A similar shift in the relaxation spectrum for the entire matrix (not just in the bundles) results in a poor correlation with experimental measurements. Although not conclusive, the comparison presented in Fig. 11 indicates that the presence of the fiber surface does influence the local mobility of the polymer matrix in the bundle region and provides motivation for further experiments to explore this exciting development.

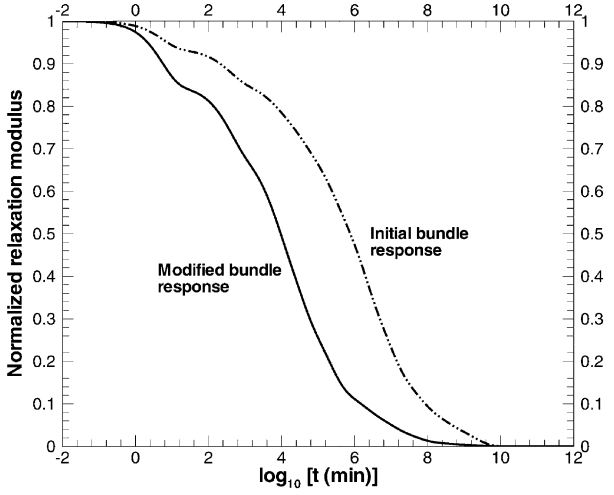

Fig. 10. Normalized initial and modified relaxation moduli of the bundles.

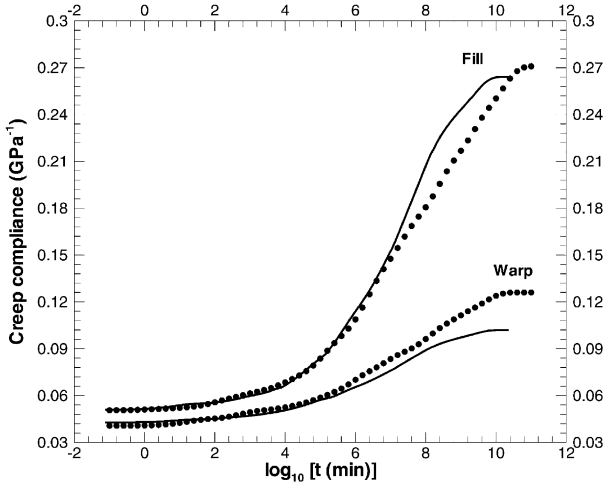

Fig. 11. Comparison of the experimental and predicted creep compliances of the plain weave composite. The symbols correspond to experimental data, and the curves represent the numerical results. The peak of relaxation spectrum of the bundles has been shifted to the left by two decades in the numerical simulation.

6.2. Deformation field

Fig. 12 plots the deformed shape of a repeating unit when applying a uniformly distributed load of 3 GPa along the warp direction at 27 °C for 10 min. The numerical results are obtained using the modified viscoelastic bundle response. Unlike traditional laminated composites, woven composites do not exhibit a uniform strain distribution under a uniform applied load. Furthermore, as evidently shown in Fig. 12, the crimped bundles tend to straighten out under tension, causing large out-of-plane warpage in the lamina. The magnitude of the out-of-plane displacement is found to be of the

Table 6
Relaxation times and weight factors used in Eq. (5) for the modified bundle response

ω	λ_ω (min)	W_ω
1	5.32	0.1483
2	3.61e2	0.1425
3	5.39e3	0.1547
4	2.53e4	0.2165
5	1.91e5	0.1891
6	1.46e6	0.0513
7	7.70e6	0.0445
8	4.25e7	0.0327
9	2.16e8	0.0064
10	1.93e9	0.0063

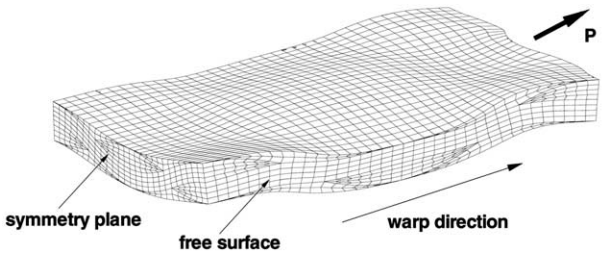

Fig. 12. Deformed shape of a repeating unit loaded along the warp direction. The boundary conditions are described in Fig. 6(b).

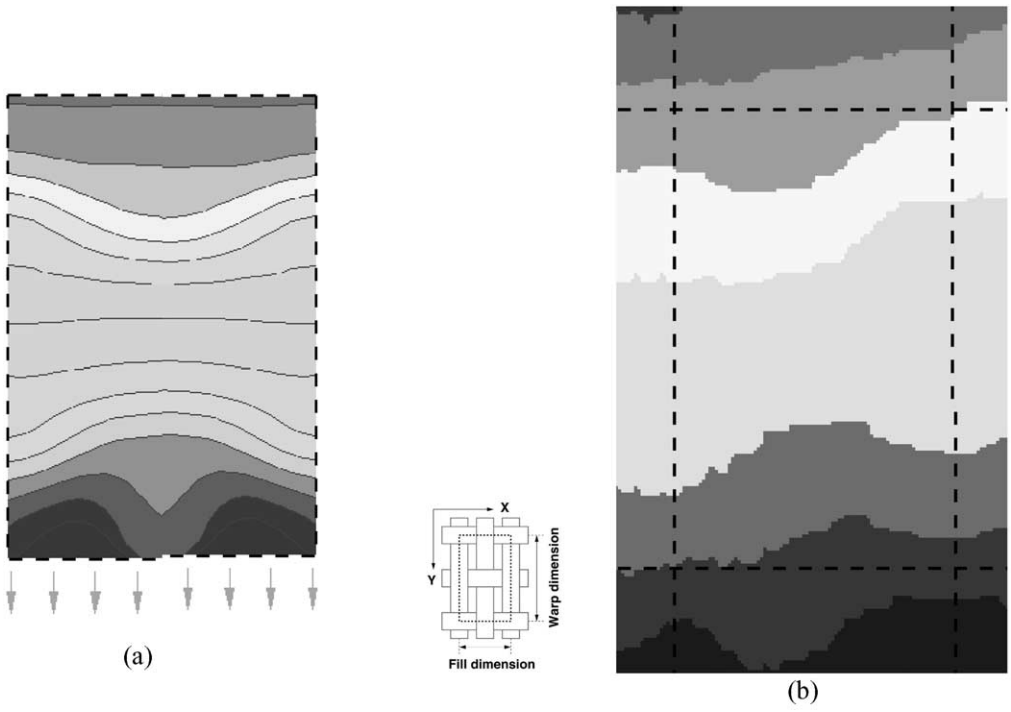

Fig. 13. Comparison between numerical and experimental displacement fields for a specimen loaded along the warp (Y) direction at 27 °C for 10 min: (a) numerical V field, (b) moiré V field.

same order as the displacement in the loading direction. Loading in the fill direction shows similar deformation pattern.

The inhomogeneity of the deformation field is further demonstrated in contour plot of displacement over the repeating unit. The numerical in-plane displacement field is compared with the moiré image reported by Shrotriya and Sottos [12,13] in Fig. 13. The moire image represents the deformation of a unit cell at the center of a specimen when loaded along the warp direction at 27 °C for 10 min. The numerical contour plot presents the deformation field of a repeating unit when loaded directly on its surface [see Fig. 6(b)] under the same time and temperature. As shown in Fig. 13, except for the region near the edge where the uniform load is applied, the shape of the contours further away from the loading edge is similar to that of the moire image. In the region far from the loading edge, the V deformation is symmetric about the centerlines of the repeating unit. The symmetry of the deformation follows from the symmetric architecture of the repeating unit. The V deformation contours are close together in the center and corners of the repeating unit where the (fill) fibers aligned to the transverse direction are closest to the surface and are spaced apart at the midpoints of the edges where the longitudinal fibers are closest to the surface.

Deformation fields in the cross section of the composite are presented in Figs. 14 and 15 for loading along the warp and fill directions, respectively. The numerical contour shape and distribution are quite similar to those of the moire fringes obtained in [12,13]. The contour patterns are characteristic of deformation associated with bending loads. These results indicate that, even under uniaxial tensile load, the unit cell is subjected to localized bending. Bending moment in the unit cell develops due to the undulations of fibers aligned in the loading direction. Furthermore, the symmetric nature of the pattern indicates that the neighboring unit cells are subjected to equal and opposite bending moments. Therefore, the total bending moment over the repeating pattern is zero in accordance to the moment equilibrium equations for the whole specimen. The contour and fringe patterns corresponding to the warp direction specimens are sparse in comparison with those for the fill direction due to lower crimp angle.

In each pair of comparable displacement fields at a given temperature [for instance, (a) vs. (c) and (f) vs. (h) in Fig. 14], each contour represents an equal increment in displacement. In the plots for both warp and fill direction specimens, the number of contours in the periodic pattern increases with increasing temperature, indicating the increase in total deformation due to relaxation of the composite. Furthermore, the contours for the displacement field along the loading direction (V for warp and U for fill) show higher inclined angles at higher temperature, indicating the increased non-homogeneity in the deformation.

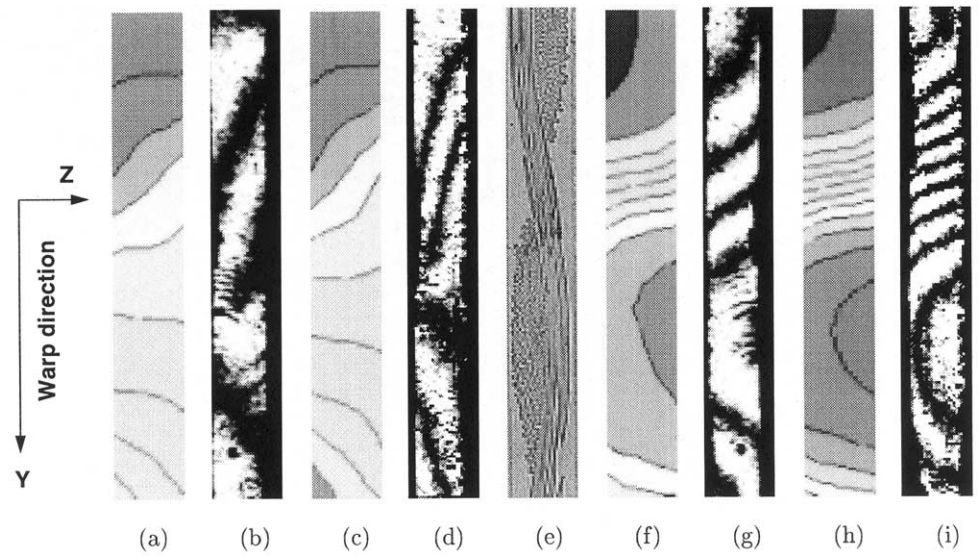

Fig. 14. Comparison between numerical and experimental displacement fields for a specimen loaded along the warp (Y) direction for 10 min: (a) numerical V field at 27 °C, (b) moiré V field at 27 °C, (c) numerical V field at 80 °C, (d) moiré V field at 80 °C, (e) composite microstructure, (f) numerical W field at 27 °C, (g) moiré W field at 27 °C, (h) numerical W field at 80 °C, (i) moiré W field at 80 °C.

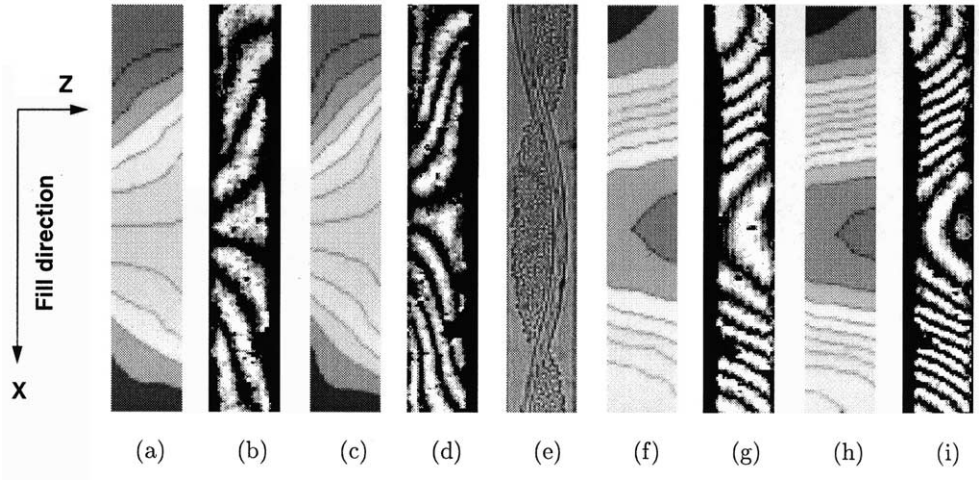

Fig. 15. Comparison between numerical and experimental displacement fields for a specimen loaded along the fill (X) direction for 10 min: (a) numerical U field at 27 °C, (b) moiré U field at 27 °C, (c) numerical U field at 80 °C, (d) moiré U field at 80 °C, (e) composite microstructure, (f) numerical W field at 27 °C, (g) moiré W field at 27 °C, (h) numerical W field at 80 °C, (i) moiré W field at 80 °C.

7. Conclusions

A 3-D viscoelastic model is utilized to predict the creep compliance of the 7628 style composite substrate for multilayer circuit board applications. The model is able to capture the initial unrelaxed compliance of the composite quite accurately. Comparisons of the model predictions with experimental data clearly indicate that the creep compliance of the composite is dependent not only on the relaxation of the matrix, but also on flexural deformations of the woven fabric bundles, and that the response of the bundle plays a major role in the viscoelastic behavior of the composite. Comparisons between 3-D and 2-D results obtained in [12] show a strong 3-D effect in the woven composites due to the complex woven architecture. Predictions approximate the general trends of experimental curves but do not accurately match the fully relaxed compliance and the retardation spectrum of the compliance curves. Differences are due to micro-mechanical relations for approximating the bundle relaxation spectrum. In order to predict the viscoelastic response of woven composites, an accurate calibration of the bundle relaxation spectrum is necessary.

The inhomogeneity of the deformation field is demonstrated in contour plots of displacement over the repeating unit, and its pattern agrees with experimental observation. The deformation fields over the cross-section of the composite indicate that neighboring unit cells are subjected to equal and opposite bending moments even when the composite is loaded in uniaxial tension. The total deformation and the inhomogeneity in the deformation field of the composite increase with the increasing temperature. But the general shape and distribution of the contours remain similar, indicating that the deformation mechanisms of the composite do not change with the relaxation of the matrix, within the temperature range investigated.

Acknowledgements

The authors gratefully acknowledge the support of NSF (grant No. DMI 96-10382) and of the Motorola Advanced Technology Group, Motorola Labs, Dr. A.F. Skipor, technical supervisor.

Appendix. Micro-mechanical relations based on self-consistent field

The generalized self-consistent field equations for longitudinal modulus, major Poisson's ratio, in-plane shear modulus, bulk modulus, and transverse modulus are taken from Ref. [28]. The relation for the transverse shear modulus is taken from Ref. [29].

- Longitudinal Young's modulus (E_1):

$$E_1 = E_{Lf}V_f + E_m(1-V) + \frac{4(\nu_{LTm}-\nu_{LTf})^2 K_{Tf}K_m G_{TTm}(1-V_f)V_f}{(K_{Tf}+G_{TTm})K_{Tm}+(K_{Tf}-K_{Tm})G_{TTm}V_f} \tag{A1}$$

- Poisson's ratio (ν_{12}):

$$\nu_{12} = \nu_{LTf}V_f + \nu_m(1-V) + \frac{(\nu_{LTm}-\nu_{LTf})(K_m-K_{Tf})G_{TTm}(1-V_f)V_f}{(K_{Tf}+G_{TTm})K_{Tm}+(K_{Tf}-K_{Tm})G_{TTm}V_f} \tag{A2}$$

- In-plane shear modulus (G_{12}):

$$G_{12} = G_m\frac{(G_{LTf}+G_m)+(G_{LTf}-G_m)V_f}{(G_{LTf}+G_m)-(G_{LTf}-G_m)V_f} \tag{A3}$$

- Transverse shear modulus (G_{23}):

$$A\left(\frac{G_{23}}{G_m}\right)^2 + 2B\left(\frac{G_{23}}{G_m}\right) + C = 0 \tag{A4}$$

where

$$A = 3V_f(1-V_f)^2\left(\frac{G_{23f}}{G_m}-1\right)\left(\frac{G_{23f}}{G_m}+\eta_f\right) + \left[\frac{G_{23f}}{G_m}\eta_m + \eta_f\eta_m - \left(\frac{G_{23f}}{G_m}\eta_m - \eta_f\right)V_f^3\right] \times \left[V_f\eta_m\left(\frac{G_{23f}}{G_m}-1\right) - \left(\frac{G_{23f}}{G_m}\eta_m + 1\right)\right], \tag{A5}$$

$$B = -3V_f(1-V_f)^2\left(\frac{G_{TTf}}{G_m}-1\right)\left(\frac{G_{TTf}}{G_m}+\eta_f\right) + \frac{1}{2}\left[\frac{G_{TTf}}{G_m}\eta_m - \left(\frac{G_{TTf}}{G_m}-1\right)V_f + 1\right] \times \left[(\eta_f-1)\left(\frac{G_{TTf}}{G_m}+\eta_f\right) - 2\left(\frac{G_{TTf}}{G_m}\eta_m - \eta_f\right)V_f^3\right] + \frac{V_f}{2}(\eta_m+1)\left(\frac{G_{TTf}}{G_m}-1\right)\left[\frac{G_{TTf}}{G_m}+\eta_f + \left(\frac{G_{TTf}}{G_m}\eta_m - \eta_f\right)V_f^3\right], \tag{A6}$$

$$C = -3V_f(1-V_f)^2\left(\frac{G_{TTf}}{G_m}-1\right)\left(\frac{G_{TTf}}{G_m}+\eta_f\right) + \left[\frac{G_{TTf}}{G_m}\eta_m + \left(\frac{G_{TTf}}{G_m}-1\right)V_f + 1\right]\left[\frac{G_{TTf}}{G_m}+\eta_f + \left(\frac{G_{TTf}}{G_m}\eta_m - \eta_f\right)V_f^3\right], \tag{A7}$$

and

$$\eta_m = 3-4\nu_m, \qquad \eta_f = 3-4\nu_{TTf} \tag{A8}$$

- Plane-strain bulk modulus (K_{23}):

$$K_{23} = \frac{(K_{Tf}-G_m)K_m + (K_{Tf}-K_m)G_mV_f}{(K_{Tf}-G_m)-(K_{Tf}-K_m)V_f} \tag{A9}$$

- Transverse Young's modulus (E_2):

$$E_2 = \left(\frac{1}{4k} + \frac{1}{4G_{23}} + \frac{\nu_{12}^2}{E_1}\right)^{-1} \tag{A10}$$

In the relations above E_p, G_p, K_p, ν_p, and V_p are Young's modulus, shear modulus, bulk modulus, Poisson's ratio, and volume fraction, respectively, and p = m or f for matrix and fiber.

References

[1] Sottos NR, Ockers JM, Swindeman M. Thermoelastic properties of plain weave composites for multilayer circuit board applications. Journal of Electronic Packaging 1999;121(1):37–43.

[2] Wu TY, Guo Y, Chen WT. Thermal-mechanical strain characterization for printed wiring boards. IBM Journal of Research and Development 1993;37(5):621–34.

[3] Yuan J, Falanga LA. The in-plane thermal expansion of glass fabric reinforced epoxy laminates. Journal of Reinforced Plastics and Composites 1993;12(4):489–96.

[4] Wang TM, Daniel IM, Gotro JT. Thermoviscoelastic analysis of residual stresses and warpage in composite laminates. Journal of Composite Materials 1992;26(6):883–99.

[5] Shrotriya P, Sottos NR. Creep and relaxation behavior of woven glass/epoxy substrates for multilayer circuit board applications. Polymer Composites 1998;19(5):567–78.

[6] Tan P, Tong L, Steven GP. Modelling for predicting the mechanical properties of textile composites-a review. Composite Part A 1997;28:903–22.

[7] Kuhn JL, Charalambides PG. Elastic response of porous matrix plain weave fabric composites: Part I—modeling. Journal of Composite Materials 1998;32(16):1426–71.

[8] Kuhn JL, Charalambides PG. Elastic response of porous matrix plain weave fabric composites: Part II—results. Journal of Composite Materials 1998;32(16):1472–507.

[9] Govindarajan S, Langrana NA, Weng GJ. An experimental and theoretical study of creep of a graphite/epoxy woven composite. Polymer Composites 1996;17(3):353–61.

[10] Ishikawa T, Chou TW. Stiffness and strength behaviour of woven fabric composites. Journal of Material Science 1982;17(11):3211–20.

[12] Shrotriya P. Dimensional stability of multilayer circuit boards. PhD thesis, University of Illinois at Urbana-Champaign, 2001.

[13] Shrotriya P, Sottos NR. Experimental investigation of woven composite deformation. Experimental Mechanics [submitted for publication].

[14] Wang TM, Danial IM, Gotro JT. Thermoviscoelastic analysis of residual stresses and warpage in composite laminates. Journal of Composite Materials 1992;26(6):883–99.

[15] Schapery RA. Stress analysis of viscoelastic composite materials. Journal of Composite Materials 1967;1(3):228–67.

[16] Taylor RL, Pister KS, Goudreau GL. Thermomechanical analysis of viscoelastic solids. International Journal for Numerical Methods in Engineering 1970;2(1):45–59.

[17] Lin KY, Yi S. Analysis of interlaminar stresses in viscoelastic composites. International Journal of Solids Structures 1991;27(7):929–45.

[18] Christensen M. Theory of viscoelasticity. New York: Academic Press; 1971.

[19] Zhu Q, Li M, Geubelle PH, Tucker III CL. Dimensional accuracy of thermoset composites: Simulation of process-induced residual stresses. Journal of Composite Materials 2001;35(24):2171–206.

[20] Zhu Q. Dimensional accuracy of thermoset polymer composites: process simulation and optimization. PhD thesis, University of Illinois at Urbana-Champaign, 2001.

[21] Naik NK. Woven fabric composites. Lancaster (PA): Technomic; 1994.

[22] Lipatov YS. Physical chemistry of filled polymers. International polymer science and technology monograph no. 2. Shrewsbury (UK): Rubber and Plastics Research Association of Great Britain; 1979.

[23] Lipatov YS, Babich VF, Rosovizky VF. Effect of filler on the relaxation time spectra of filled polymers. Journal of Applied Polymer Science 1976;20:1787–94.

[24] Crowson RJ, Arridge RGC. The elastic properties in bulk and in shear of a glass bead reinforced epoxy resin composite. Journal of Material Science 1977;12:2154–64.

[25] Palmese GR, McCullough RL. Effect of epoxy-amine stoichiometry on cured resin material properties. Journal of Applied Polymer Science 1992;46:1863–73.

[26] Sottos NR, Swindeman M. Transient thermal deformations of the interphase in polymer composites. Journal of Adhesion 1995;53:69–78.

[27] Sullivan JL, Wen YF, Gibson RF. Universal aspects of composite viscoelastic behavior. Polymer Composites 1995;16(1):3–9.

[28] Whitney JM, McCullough RL. Micromechanical materials modeling, Delaware Composites Design Encyclopedia. Lancaster (PA): Technomic; 1990.

[29] Christensen RM. A critical evaluation for a class of micromechanics models. Journal of Mechanics and Physics of Solids 1990;38(3):379–404.